

Dynamic fluid configurations in steady-state two-phase flow in Bentheimer sandstone

Ying Gao ,* Ali Q. Raeini, Martin J. Blunt , and Branko Bijeljic

*Qatar Carbonates and Carbon Storage Research Centre, Department of Earth Science and Engineering,
Imperial College London, London SW7 2AZ, United Kingdom*

(Received 27 March 2020; revised 29 July 2020; accepted 29 December 2020; published 25 January 2021)

Fast synchrotron tomography is used to study the impact of capillary number, Ca , on fluid configurations in steady-state two-phase flow in porous media. Brine and n -decane were co-injected at fixed fractional flow, $f_w = 0.5$, in a cylindrical Bentheimer sandstone sample for a range of capillary numbers $2.1 \times 10^{-7} \leq \text{Ca} \leq 4.2 \times 10^{-5}$, while monitoring the pressure differential. As we have demonstrated in Gao *et al.* [Phys. Rev. Fluids **5**, 013801 (2020)], dependent on Ca , different flow regimes have been identified: at low Ca only fixed flow pathways exist, while after a certain threshold dynamic effects are observed resulting in intermittent fluctuations in fluid distribution which alter fluid connectivity. Additionally, the flow paths, for each capillary number, were imaged multiple times to quantify the less frequent changes in fluid occupancy, happening over timescales longer than the duration of our scans (40 s). In this paper we demonstrate how dynamic connectivity results from the interaction between oil ganglia populations. At low Ca connected pathways of ganglia are fixed with time-independent small, medium, and large ganglia populations. However, with an increase in Ca we see fluctuations in the size and numbers of the larger ganglia. With the onset of intermittency, fluctuations occur mainly in pores and throats of intermediate size. When Ca is further increased, we see rapid changes in occupancy in pores of all size. By combining observations on pressure fluctuations and flow regimes at various capillary numbers, we summarize a phase diagram over a range of capillary numbers for the wetting and nonwetting phases, Ca_w and Ca_{nw} , respectively, to quantify the degree of intermittent flow. These different regimes are controlled by a competition between viscous forces on the flowing fluids and the capillary forces acting in the complex pore space. Furthermore, we plot the phase diagrams of the transition from Darcy flow to intermittent flow over a range of Reynolds and Weber numbers for the wetting and nonwetting phases to evaluate the balance among capillary, viscous, and inertial forces, incorporating data from the literature. We demonstrate that pore geometry has a significant control on flow regime.

DOI: [10.1103/PhysRevE.103.013110](https://doi.org/10.1103/PhysRevE.103.013110)

I. INTRODUCTION

Multiphase flow through geological porous media occurs in a wide range of processes of global importance, such as oil and gas production from hydrocarbon reservoirs, flow in aquifers, and underground carbon dioxide storage [1–4]. While single-phase flow has been well characterized, many phenomena of steady-state immiscible two-phase flows—here oil and water—in porous media are still not well understood. The macroscopic flow of immiscible phases in porous rock is determined by complex microscopic processes. These processes are governed by the competition between viscous and capillary forces, which depends on the geometry and topology of the pore structure, as well as wettability and flow regime [4].

Generally, both capillary and viscous forces control the flow behavior. To quantify the ratio of capillary to viscous forces we define capillary number as $\text{Ca} = q_t \mu / \sigma$, where q_t is the total Darcy velocity of the two fluids, $q_t = q_w + q_o$, σ is the interfacial tension between the wetting phase (water in this paper) and the nonwetting phase (oil), and μ is the average viscosity of the two phases.

The first studies of the effect of viscous and capillary forces on multiphase flow were performed in micromodels where a transparent two-dimensional lattice of channels represented the porous medium [5,6]. These works identified the importance of time-dependent fluctuations in pore-scale occupancy, which was termed ganglion dynamics [5,6]. Later studies quantified flow regimes in steady-state simultaneous two-phase flow [7–9]. Oil fragmentation and mixing were observed at high capillary numbers. The pressure drop was recorded and a nonlinear power-law relationship between the pressure gradient and the capillary number was observed: this is different from the traditional Darcy-law formulation of flow in porous media which assumes a linear relationship between flow rate and pressure gradient. The nonwetting phase saturation decreased when Ca increased [7–9]. In three dimensions, confocal microscopy has been used to study flow regimes in a bead pack [10,11]. A transition from flow in fixed flow pathways to more dynamic displacement with fluctuating fluid pathways was observed with an increase in Ca .

The development of x-ray micro-computed tomography (micro-CT) provides opportunities to observe three-dimensional two-phase flow processes directly at the pore (micron) scale using either laboratory micro-CT or synchrotron tomography, which provides a better time resolution [12]. Ganglion dynamics, involving the disconnection and

*y.gao15@imperial.ac.uk

reconnection of clusters of the nonwetting phase surrounded by the wetting phase, has been observed using fast synchrotron-based x-ray micro-CT in a sintered glass bead pack during the simultaneous flow of two phases [13]. Furthermore, the onset of oil mobilization was seen in a sandstone sample during imbibition, in which both connected pathway flow and ganglion dynamics occurred [14–16]. Later, dynamic changes in connectivity were observed by Reynolds *et al.* [17] at low Ca in a Bentheimer sandstone for a brine-N₂ system. Using differential x-ray tomography in a laboratory micro-CT, Gao *et al.* [18] observed intermittent pore occupancy during simultaneous injection of decane and brine in a Bentheimer sandstone for a capillary number, $Ca = 7.5 \times 10^{-6}$, while fixed pathway flow was seen for a lower capillary number, $Ca = 3.0 \times 10^{-7}$. Using the same method, Gao *et al.* [19] confirmed intermittency in Estaillasses limestone at $Ca = 7.3 \times 10^{-6}$ and observed that the intermittency is principally seen in the smaller and intermediate-sized pores and throats. Furthermore, Spurin *et al.* [20,21] studied various fluid pairings and capillary numbers using laboratory-based micro-CT in Estaillasses limestone. They observed that intermittency occurs in intermediate-sized and poorly connected pores.

However, a full understanding of the mechanisms governing flow behavior as a function of flow rate is still lacking. Intermittency is not a manifestation of nonwetting phase ganglia advecting through the pore space, as considered in previous work [5,6], but occurs when the nonwetting phase forms temporary pathways to increase its conductance, akin to cars controlled by traffic lights [17]. The physical origin of this effect is the extra energy injected as the flow rate increases which allows the formation of additional interfaces in the pore space [22].

In this paper, we study displacement mechanisms in steady-state two-phase flow at a range of flow rates covering conditions typically encountered in the subsurface, and provide additional analysis of the experimental data from Gao *et al.* [22]. In this recent work [22], when the capillary number was increased from 2.1×10^{-7} to 4.2×10^{-5} , we observed fluid displacements with complex interface dynamics in three flow regimes: regime 1 for $Ca < 10^{-6}$ was capillary dominated, regime 2 beyond $Ca^* \approx 10^{-6}$ was characterized by the onset of dynamics, while regime 3 for $Ca > Ca^* \approx 10^{-5}$ was defined as the intermittent flow regime with a nonlinear relationship between flow rate and pressure gradient. In this paper, we will analyze the pore-scale images to elucidate the mechanisms by which this intermittency occurs.

At comparatively low flow rates, the fluids flow through fixed pathways, consistent with the traditional theory of multiphase flow based on an empirical extension of Darcy's law [4]:

$$q_i = -\frac{k_{r,i}k}{\mu_i}(\nabla P_i - \rho_i g), \quad (1)$$

where q [m/s] is the Darcy velocity for phase i , which is the volume of fluid flowing per unit cross-sectional area of the porous medium per unit time, k [m²] is the absolute permeability, μ_i [Pa s] is the dynamic viscosity for phase i , ∇P_i [Pa] is the pressure gradient, ρ_i [kg/m³] is the fluid density, g [m/s²] is the acceleration due to gravity, and $k_{r,i} < 1$ is the relative permeability for phase i . Generally, the sum of relative permeabilities over all phases is less than 1, since fluid

menisci block the flow. However, after some critical value of Ca^* , we start to see dynamics which we define as fluctuating occupancy where—during steady-state flow—some regions of the pore space are periodically occupied by both phases. At these high flow rates this linear relationship between pressure gradient and flow rate may not hold.

The main objective of this study is to quantify, for the range of Ca studied, the following: (1) change in fluid configurations over timescales larger than the scan duration, (2) where in the pore space intermittency occurs at timescales below the time resolution of the scans, and (3) relate these phenomena to observed relationship between flow rate and pressure gradient. Furthermore, we will draw a comparison of the synchrotron- and laboratory-based experiments to delineate the capabilities of the two methods and provide insights into the impact of the capillary number on the flow regimes. Finally, we will generalize our results including previously published data through a phase diagram that characterizes intermittency across flow regimes as a function of Ca for different porous media.

II. MATERIALS AND EXPERIMENTAL METHODS

In this work, three sets of two-phase co-injection experiments at steady state, by both synchrotron-based and laboratory-based micro-CT, were performed on a Bentheimer sandstone sample at different flow rates. Bentheimer sandstone was chosen for its homogeneous pore structure. More details of these experiments can be found in Gao *et al.* [22]. The details of the experiments are as follows:

(1) Decane and brine co-injection for $f_w = 0.5$ at 0.02 ml/min, 0.04 ml/min, 0.08 ml/min, 0.4 ml/min, 0.8 ml/min, 1.2 ml/min, 2.5 ml/min, and 4 ml/min. The experiments were performed using fast synchrotron tomography at a time resolution of 1 min.

(2) Decane and brine co-injection at 0.02 ml/min for $f_w = 0.5$. The observations from this experiment are called the low Ca observations. The experiment was carried out using laboratory-based micro-CT at a time resolution of 1 h.

(3) Decane and brine co-injection at 0.5 ml/min for $f_w = 0.5$. These represent the high Ca observations. The experiment was performed using laboratory-based micro-CT at a time resolution of 1 h.

A. Experiments conducted using synchrotron-based micro-CT

The experiments were conducted on Bentheimer sandstone with a porosity of $20.0\% \pm 0.4\%$ obtained from the micro-CT image. The sample was a cylinder (called a core) 6.01 ± 0.01 mm in diameter and 57.11 ± 0.01 mm in length. The relatively long core was used to minimize capillary end effects, and only the middle part (with a length of 5.2 mm) was scanned. A solution of 15 wt% brine, doped with potassium iodide (KI), was used as the wetting phase, which had a high contrast with the nonwetting phase. The viscosity of brine is 0.83 ± 0.01 mPa s. Decane was used as the nonwetting (oil) phase, whose viscosity is 0.838 mPa s (provided by PubChem, open chemistry database). Using the pendant drop method [23,24], the interfacial tension between brine and decane was measured to be 45.72 ± 1.76 mN/m at ambient conditions measured by a Rame-Hart apparatus (590 F4 series).

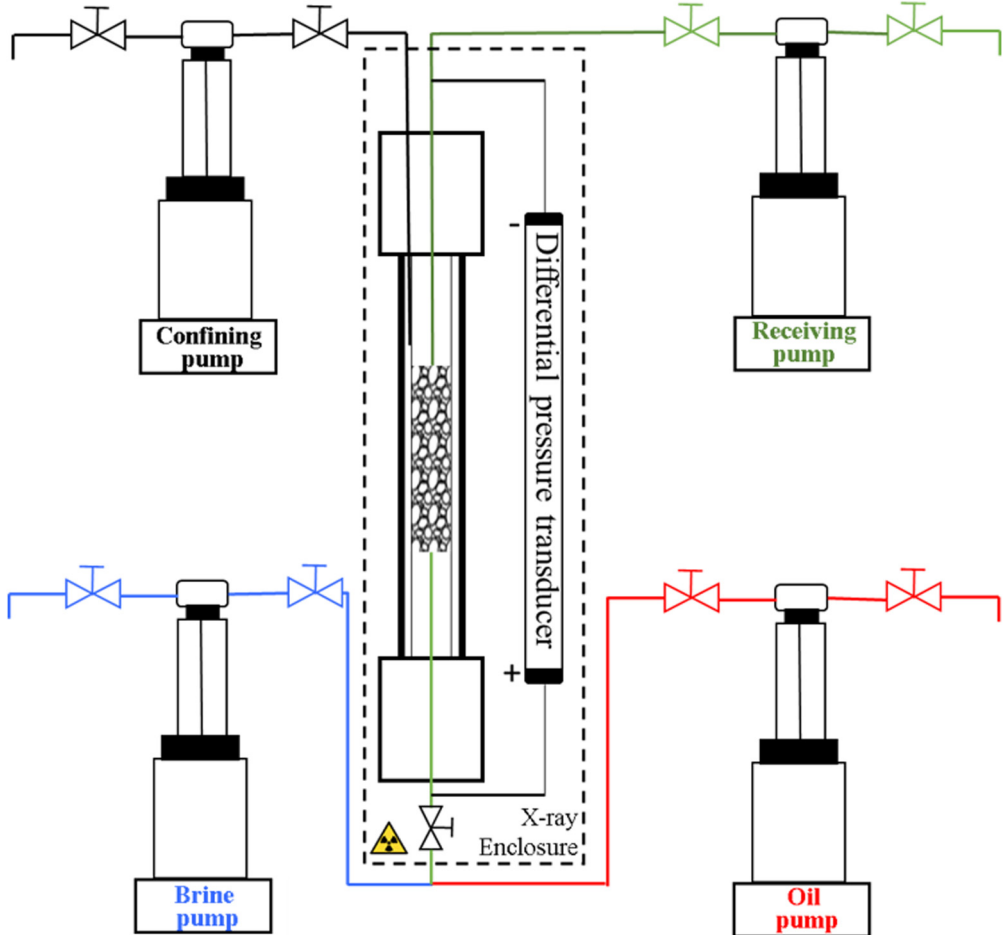


FIG. 1. The experimental apparatus consisted of four pumps: oil and brine injecting pump controlling flow, the receiving pump controlling back pressure, and a confining pump controlling confining pressure on a Viton confining sleeve within the carbon fiber sleeve of the Hassler cell to avoid fluid bypass. The rock sample was placed into a Viton sleeve and attached to flow lines within the Hassler cell. The Hassler cell was mounted vertically on the rotation stage.

Two-phase experiments were performed at steady state through the flow apparatus shown in Fig. 1. The pumps were Teledyne ISCO Syringe pumps: a 100DX high syringe pump for low flow rates and a 1000D high-pressure syringe pump for flow rates higher than 0.1 ml/min. The stepping motor of the 100DX pump injects 9.65 nl/step. When the total flow rate was 0.02 ml/min, the brine flow rate was 0.01 ml/min and there were 17 steps of the pump per second, which was more frequent than the scan resolution, 1 scan per minute. The displacement resolution of 1000D was 25.38 nl/step. When the total flow rate was 0.8 ml/min, the brine flow rate was 0.4 ml/min and there were 263 steps per second. This indicates that the stepping motor was much more rapid than the scan times and so were unlikely to affect the images we obtained. A more detailed description of the experimental procedure is given in Gao *et al.* [22].

Three-dimensional images were taken every 1 min, including 40 s to take 1000 projections and 20 s to rotate the sample stage back to 0° and transfer the data to a computer. The field of view of camera was $6.7 \times 5.6 \text{ mm}^2$, giving a reconstructed image of 1000^3 voxels with a voxel size of $5.2 \mu\text{m}$. The images were processed using commercial image analysis software [25]. All reconstructed images were registered to the

dry scan image to correct small movements caused during the scans. Then the Lanczos algorithm was used to resample them to the same orientation to describe the differences associated with different flow regimes accurately [26,27]. The differential imaging method [19,28] was applied to obtain difference images between the image saturated with brine and the image with two-phase flow, by which to identify regions of the pore space filled intermittently. If there is no intermittency in the raw image, there are only two grayscale values—black and white—in the differential image, which applies to the images taken in flow regimes 1 and 2. Instead, if there is intermittency in the raw image, caused by changes in fluid occupancy during the time of a single scan, one or more intermediate grayscale values can be identified in the differential image, as seen in flow regime 3. The nonlocal means filter was applied on the raw images to smooth the difference images [29,30]. Watershed segmentation was used to extract the oil phase from all experimental images.

An illustration of the steps in segmentation is shown in Fig. 2. Figure 2(b) shows the image taken when oil and water phases flow through fixed pathways at $\text{Ca} = 4.2 \times 10^{-7}$. At higher flow rates, in regime 3, we observed an intermittent phase with an intermediate grayscale: here during the 60 s

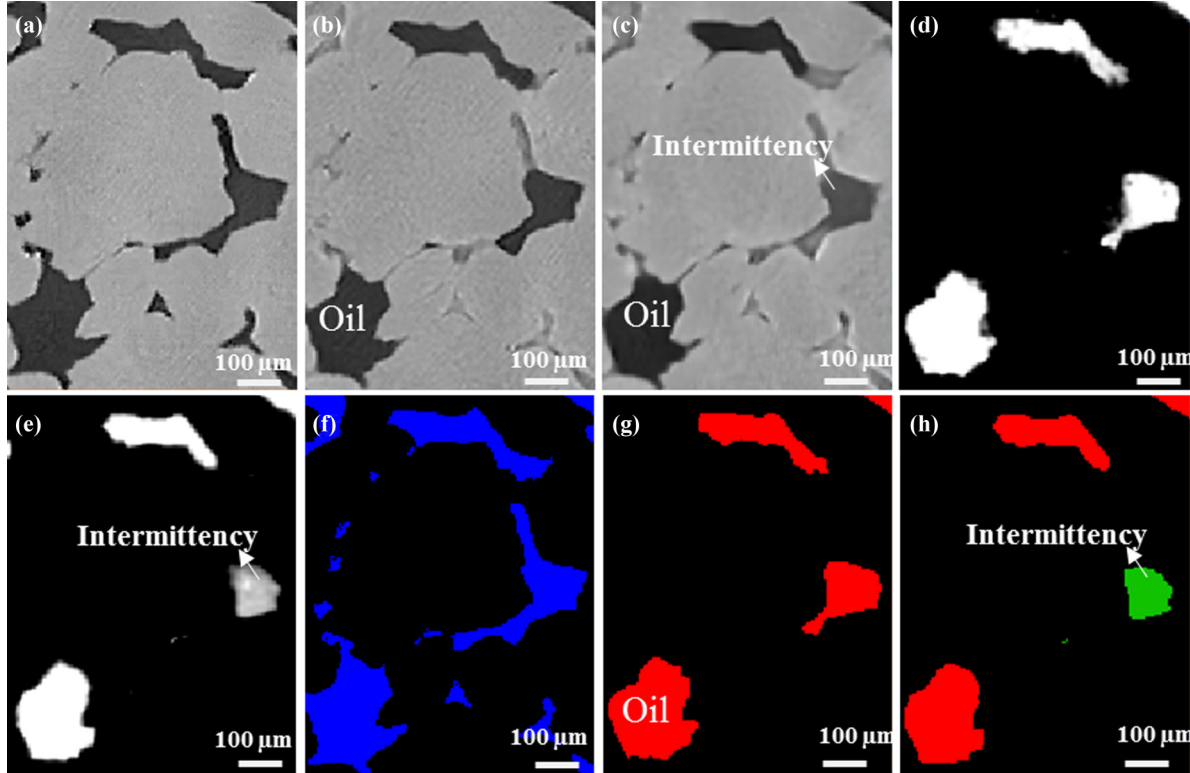


FIG. 2. Illustration of the steps performed in segmentation. (a) An example pore space from the dry scan. (b) The same pore space imaged during flow when $\text{Ca} = 4.2 \times 10^{-7}$. (c) The same pore space imaged when $\text{Ca} = 2.6 \times 10^{-5}$. (d) Differential image between the pore space imaged when brine is fully saturated and (b) after normalization. (e) Differential image between the pore space imaged when brine is fully saturated and (c) after normalization. (f) The pore segmentation. (g) Segmented oil phase in the pore space when $\text{Ca} = 4.2 \times 10^{-7}$. (h) Segmented oil and intermittency in the pore space when $\text{Ca} = 2.6 \times 10^{-5}$. Red is oil. Green represents intermittent occupancy identified by an intermediate grayscale in the pore space.

timescale of the scan some voxels were occupied for some time by water and some time by oil.

Figure 2(c) shows the image taken when **intermittent phase** appears in the pore space at $\text{Ca} = 2.6 \times 10^{-5}$. The oil phase is highlighted in the pore space in the difference images in Fig. 2(d).

B. Experiments conducted using laboratory-based micro-CT

The porosity measured from our micro-CT image was $22.0\% \pm 0.5\%$. The rock samples used were 4.99 ± 0.01 mm in diameter and 60.0 ± 0.01 mm in total length. The wetting phase was 30 wt% KI brine with a viscosity of 0.83 ± 0.01 mPa s, while the nonwetting, oil, phase was again *n*-decane. Using the same methods as mentioned above, the interfacial tension was measured as 47.05 ± 1.56 mN/m at ambient conditions.

The experimental apparatus was shown in Fig. 1. The procedures and **more detail on the experimental protocol can be found in Gao *et al.* [18]**.

III. RESULTS AND DISCUSSION

The flow regimes were characterized through a series of experiments over a range of flow rates using fast synchrotron tomography. In this section, the dynamic connectivity of the nonwetting phase (Sec. III A), the dynamic saturation pro-

file of the wetting phase (Sec. III B), and pore and throat occupancy of brine, oil, and intermittent regions (Sec. III C) are analyzed for the wide range of Ca in the three flow regimes, and their variations between different repeated scans are quantified. In Sec. III D we compare the results obtained by synchrotron and laboratory micro-CT experiments, and in Sec. III E we provide further quantitative analysis of the flow regimes.

A. Dynamic connectivity of the nonwetting phase

The pore-scale details of dynamic connectivity of the nonwetting phase are shown in Fig. 3. In this figure, the oil phase is connected through a complex pore space at low $\text{Ca} = 2.1 \times 10^{-7}$. However, the nonwetting phase moves intermittently through some smaller throats (restrictions in the pore space) occasionally at high Ca. Figure 3(b) shows that the oil phase was connected when $\text{Ca} = 8.3 \times 10^{-6}$, while it was disconnected 10 min later; see Fig. 3(c). At the lowest flow rates, fluid configurations are governed entirely by capillary effects and remain fixed over time. We begin to see some local rearrangement of the fluids, which we call intermittency, at around $\text{Ca} \approx 10^{-6}$.

In our previous work [22] we observed two types of fluctuation: the first, called type 1, was when we saw a distinct change in the phase occupying a voxel from one scan to the next, as shown in Fig. 3. This represented a change in

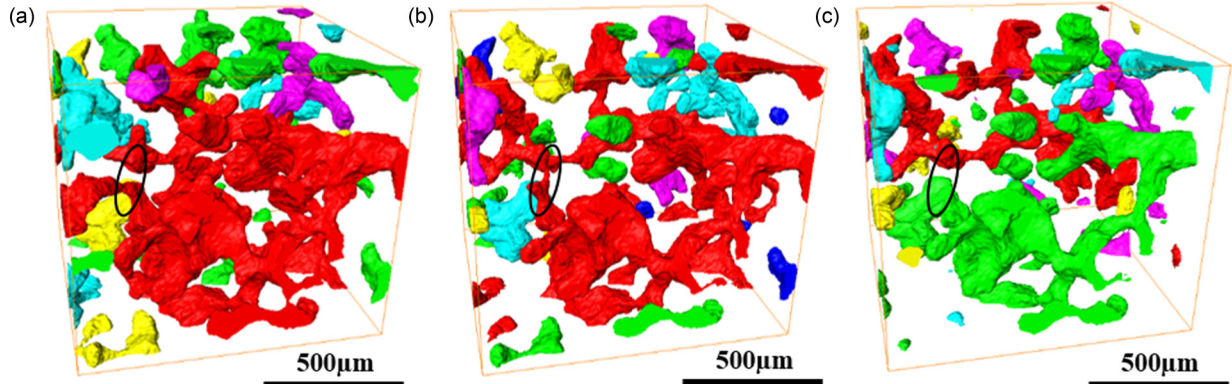


FIG. 3. 3D configuration of oil ganglia in a selected region of the pore space of Bentheimer sandstone. The colors indicate different discrete clusters of oil. (a) For $\text{Ca} = 2.1 \times 10^{-7}$, the red cluster represents that oil flows through connected pathway from bottom to top. Oil occupies only large pores with no connection in the marked black ellipse. (b) For $\text{Ca} = 8.3 \times 10^{-6}$, the oil has sufficient energy to open up the shortcut where the pore space has a narrower inscribed radius. (c) The oil configuration in the same region of the pore space imaged 10 min after (b) at the same capillary number, which shows that the connection has been temporarily broken.

fluid configuration that occurred over a timescale of 1 min or more. The second behavior, called type 2, was when the fluctuations were rapid enough to occur within 1 min, shown in Fig. 2. In this case we observed an intermediate grayscale value between water and oil occurring in one voxel instead of clear changes. Here we will quantify what this means in terms of ganglia populations.

Figure 4 shows the interactions between ganglia populations of the segmented nonwetting (oil) phase at low and high Ca . Here we consider flow regimes 1 and 2. Figure 4(a) shows the saturation profile for the last 30 min at steady state when $\text{Ca} = 2.1 \times 10^{-7}$, while Fig. 4(b) shows the saturation profiles for the last 30 min at steady state when $\text{Ca} = 8.3 \times 10^{-6}$. To visualize the connectivity clearly, the ganglia populations were subdivided into three classes and as shown with different colors in Fig. 4(c): large ganglia in green, containing thousands of pores and that may span across the field of view with more than 10^7 voxels; medium ganglia in red, which may be connected over tens to hundreds of pores, ranging from 10^5 to 10^7 voxels; and small ganglia in blue, which may be isolated in a single pore or be simply connected over a few pores, ranging from 5000 to 10^5 voxels. Ganglia smaller than 5000 voxels, which had volumes less than one single pore, were ignored in this analysis. Figure 4(c1) shows the volume rendering of oil ganglia at the low capillary number of 2.1×10^{-7} at time 1 in Fig. 4(a) to contrast the volume renderings of oil ganglia shown in Figs. 4(c2) and 4(c3) for the high capillary number of 8.3×10^{-6} at times 2 and 3 shown in Fig. 4(b). We do not consider the ganglion population in regime 3 since here we cannot distinguish discrete ganglia because of type 2 intermittency during a scan.

We observe that at low flow rates, in flow regime 1, connected pathways of ganglia appear to be static. Moreover, the proportions of small, medium, and large ganglia stay constant over time. Again, this is consistent with flow through fixed, connected pathways.

At the higher flow rates, in regime 2, the onset of dynamics, the pore-scale configuration of fluids changes over time, as do the fractions of the oil saturation in ganglia of different size. However, in a macroscopic sense, steady state

has been reached, since the average saturations [Fig. 4(d)] are approximately constant in both space and time. If steady state had not been achieved, the entire profile would have been expected to shift with each time step. This demonstrates that, although the oil saturation remains constant, the connectivity of the nonwetting phase periodically rearranges. The interaction between the ganglia populations observed at higher flow rates is the result of alterations in dynamic connectivity. In addition, more disconnection and reconnection events occurred when the flow rate was increased, and the pathways have increasingly dynamic connectivity. We observe that few changes happen when Ca is less than 10^{-6} within the errors in our segmentation; when Ca is larger than $\text{Ca}^* \approx 10^{-6}$ some definite changes occur, while when $\text{Ca} > \text{Ca}^i \approx 10^{-5}$, in the intermittent flow regime 3, there are significant fluctuations in occupancy, which occur over timescales of less than 1 min and lead to a nonlinear relationship between flow rate and pressure gradient.

To characterize the topology of the ganglia of the nonwetting phase for different flow regimes, the Euler characteristic of the nonwetting phase was calculated for the last 30 images at each capillary number. The Euler characteristic is defined from the Betti numbers

$$\chi = \beta_0 - \beta_1 + \beta_2, \quad (2)$$

where χ is the Euler characteristic, and β represents a Betti number [4,12,31]. β_0 is the number of oil ganglia without holes, β_1 is the number of the redundant loops through pore throats within an individual ganglion, and β_2 is the number of isolated regions of the wetting phase surrounded by oil. We do not include voxels containing intermittent flow in regime 3 as part of the nonwetting phase.

Figure 5 shows the Euler characteristic per unit volume for 30 3D images at each capillary number as a function of water saturation. As Ca increases there is a small increase in water saturation—the saturation of the nonwetting phase decreases. The Euler characteristic initially decreases with Ca in regime 2, the onset of dynamics, indicating better connectivity. This is a surprising result, as Fig. 4 appears to show an increase in the number of small ganglia and fewer large ganglia in

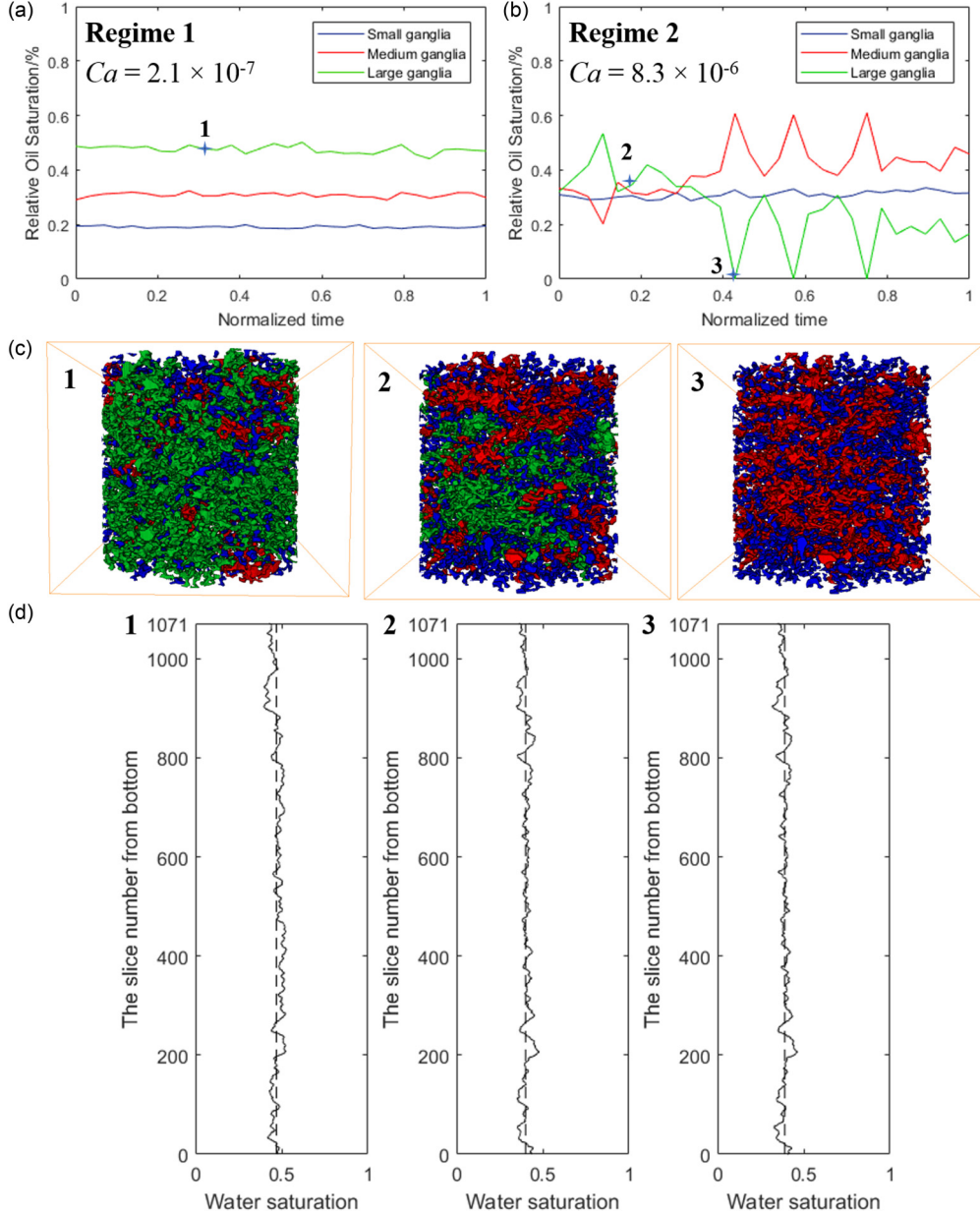


FIG. 4. Interaction between oil ganglia populations in regimes 1 and 2. The plots show the relative oil saturation of small (blue/black), medium (red/dark gray), and large (green/light gray) ganglia when $Ca = 2.1 \times 10^{-7}$ (a) and 8.3×10^{-6} (b). (c) Sample volume renderings of oil ganglia, which correspond to the numbers shown in (a) and (b). Flow is from bottom to top. (d) Sliced-averaged brine saturation distribution profile along the whole sample corresponding to the numbers shown in (a) and (b).

regime 2. However, the nonwetting phase rearranges itself in the pore space to allow better connectivity to facilitate flow; furthermore this analysis considers ganglia of all size, while the smaller ganglia were not considered in Fig. 4. In contrast, in regime 3 for $Ca > 10^{-5}$, the nonwetting phase breaks up into smaller clusters and the Euler characteristic increases: here flow of the nonwetting phase is maintained through fluctuating pathways, and at any instant the nonwetting phase appears more poorly connected, with the larger ganglia broken up into smaller fragments.

Armstrong *et al.* [31] have also studied the Euler characteristic from both pore-space images and simulation for the simultaneous flow of a wetting and nonwetting phase through

a sintered glass bead pack over a range of fractional flows. In their work the nonwetting phase appeared more connected with a negative Euler characteristic, whereas our values are always positive. However, they observed the same trends in behavior: for lower water saturations they saw a decrease in Euler characteristic with flow rate and fewer discrete ganglia, whereas at higher water saturation, an increase in Ca led to the break up of ganglia and an increase in Euler characteristic. It is to be expected that the Euler characteristic of the nonwetting phase would be lower for glass beads since a granular pack has a highly connected pore space with more throats associated with each pore body than the sandstone studied here.

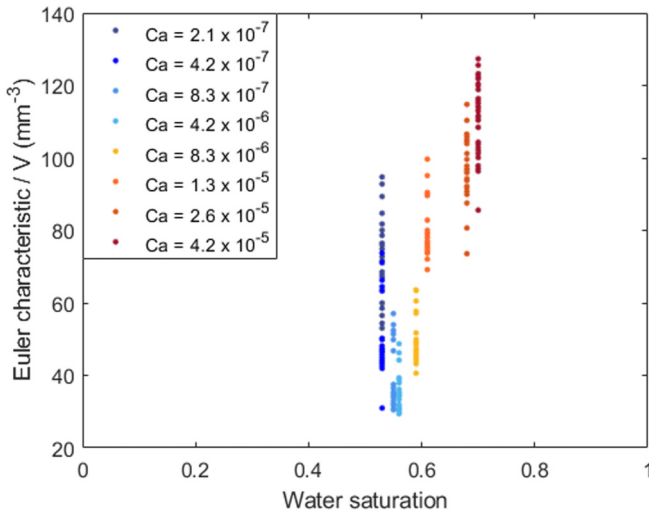


FIG. 5. The Euler characteristic per unit volume over the last 30 min at steady state as a function of water saturation for different capillary numbers. From left to right, the capillary number increases.

B. Saturation profile of the wetting phase

For regimes 1 and 2, water saturation was calculated based on the segmented images. For regime 3, the water saturation includes water that always occupied the pore space and the water fraction in the intermittent region (type 2), which was assumed to be 0.5 in this study. The water saturations calculated at each capillary number are listed in Table I. Figure 6 shows that initially when the capillary number increases, the saturation remains constant within the uncertainty in the measurements at the lowest flow rates, which are capillary dominated. However, we observe a small increase in water saturation when Ca is larger than 10^{-6} , followed by a more significant change in the intermittent flow regime. Since the fractional flow is fixed, this means that the nonwetting phase has a relatively higher conductance at the higher flow rates, since it can sustain the same fractional flow with lower saturations.

For each flow rate, steady-state conditions are confirmed by the constant brine saturation achieved in each experiment. Brine saturations calculated from the last 30 min at each capillary number at steady state are shown in Fig. 7. We see the emergence of significant changes in saturation at the higher flow rates with rapid fluctuations over time.

Analyzing the results for the brine saturation at the capillary numbers shown in Fig. 6 and the saturation data during the last 30 min shown in Fig. 7, we conclude that at the low capillary numbers in regime 1, there is little change in water saturation, within the uncertainty in the measurements. In regime 2, there is a small shift in saturation, and we observe an onset of dynamic effects from pressure fluctuations [22] and

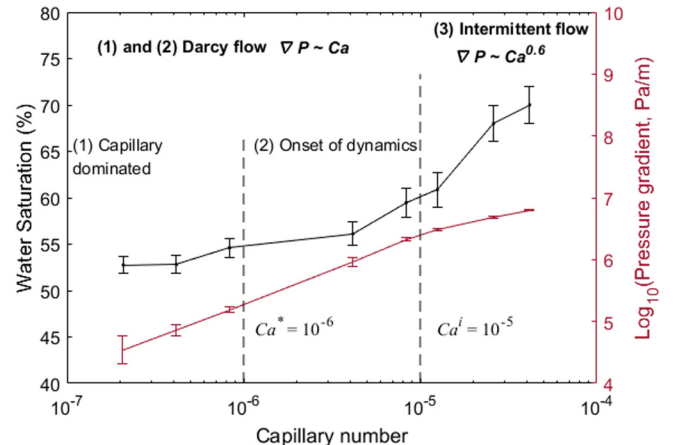


FIG. 6. Black (upper) line: Saturation of the wetting phase as a function of the capillary number at a fixed fractional flow. Water saturation remains constant for $Ca \leq Ca^*$, increases with Ca for $Ca^* < Ca \leq Ca^i$, and further increases with a larger gradient for $Ca > Ca^i$. The uncertainty in saturation is approximately 0.015 (see Table I): this was calculated by considering segmentation uncertainties as well as the standard deviation of the water saturations of 30 scans for each capillary number. Red (lower) line: Experimentally measured pressure gradient as a function of capillary number plotted on base-10 logarithmic axes. The error bars reflect the standard deviation in the pressure measurements and the measurement accuracy.

local rearrangements of the fluids in the pore space images. At the highest flow rates in regime 3, we observe more frequent dynamic rearrangements of the pore space.

C. Pore and throat occupancy

Pore occupancy determines flow and recovery encapsulated in the relative permeabilities. Generally, the oil phase occupies the larger pores because Bentheimer sandstone is strongly water-wet [4]. The location and size of the pores and/or throats where dynamic connectivity of oil ganglia occurs are investigated in this section. A generalized pore network extraction algorithm [32] was applied to subdivide the void space into pores representing wider regions and throats representing narrow restrictions between the pores based on the radii of spheres inscribed in the pore space. Then the volume fraction of pores and throats whose center were occupied by brine, oil, or intermittency were computed using these micro-CT images of fluid phases. Furthermore, by computing pore-by-pore occupancy over all experimental images taken during the last 20 min at steady state, the standard deviations were calculated for each pore and throat. Then the average standard deviations of individual pore occupancy were plotted for different bins of pore and throat size (inscribed radius)

TABLE I. Calculated water saturation at each capillary number.

| $Ca \times 10^{-7}$ | 2.1 | 4.2 | 8.3 | 42.0 | 83.0 | 130 | 260 | 420 |
|----------------------|-------|-------|-------|-------|-------|-------|-------|-------|
| Mean S_w | 0.53 | 0.53 | 0.55 | 0.56 | 0.59 | 0.61 | 0.68 | 0.70 |
| Uncertainty in S_w | 0.009 | 0.010 | 0.011 | 0.013 | 0.016 | 0.019 | 0.020 | 0.020 |

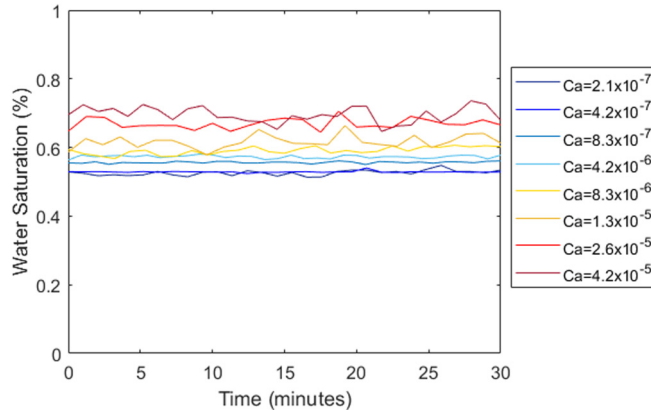


FIG. 7. Average brine saturation versus time during the last 30 min of steady-state experiments at different flow rates. The brine saturation fluctuates with time. The uncertainty in the measurements is approximately ± 0.015 . From bottom to top, the capillary number increases.

and for the experiments at different capillary numbers. This reflects the amount of temporal variation in individual pore and throat occupancy as a function of pore radius and capillary number.

As evident in Fig. 8, the oil occupies the large pores while brine resides in the corners of large pores, small pores, and throats, as expected for a water-wet medium [33]. When the capillary number is low, the oil and brine phases remained in their own fixed pathways and little change occurs. In regime 2, for $Ca > 10^{-6}$, we begin to see more significant changes in occupancy of type 1 in mainly the smaller pores. When the capillary number is increased to 10^{-5} , these changes are more significant and occur in the pores and throats of intermediate and small size. While these fluctuations tend to reduce the number of larger ganglia (see Fig. 4), the overall effect is an increase in nonwetting phase connectivity as evident from the Euler characteristic (Fig. 5).

When the capillary number is very high, larger than 10^{-5} in the intermittent flow regime 3, we observe some intermittent regions of the pore space, filled with oil and brine occasionally within the 1 min scan (see Fig. 3), which means that there is dynamic or intermittent connectivity during fluid flow. Compared with the pore occupancy at low capillary numbers, intermittent flow occurs in a larger range of pore and throat sizes at higher capillary numbers: indeed, we now see changes in some of the larger pores as well. This leads to significant break-up of larger ganglia and a decrease in the nonwetting phase connectivity, seen in Fig. 5.

D. Comparison between synchrotron and laboratory-based micro-CT

We now compare our synchrotron results with the results reported in Gao *et al.* [18]. In the latter study, we injected both oil and brine in Bentheimer sandstone using laboratory-based micro-CT at two capillary numbers: 3.0×10^{-7} and 7.5×10^{-6} . Each scan took approximately 1 h with a voxel size of $6 \mu\text{m}$. For the low capillary number of 3.0×10^{-7} , we observed connected and stable pathways. The water saturation

was 0.52 when the fractional flow was 0.5. For the high capillary number of 7.5×10^{-6} , we observed intermediate grey-scale regions occupied by both oil and water, called intermittency, during a 1 h scan. When the fractional flow was 0.5, the water saturation was 0.56 and the percentage of intermittency in macropores was 33%.

In the synchrotron-based work, at the low capillary number of 2.1×10^{-7} , two-phase flow had fixed pathways with no intermittency, consistent with our micro-CT results, while the water saturation was 0.53, similar to 0.52 seen for the laboratory-based micro-CT at a similar capillary number. At a high capillary number of 8.3×10^{-6} , we saw a clear change in the pore occupancy from one scan to the next. The corresponding water saturation at this capillary number was 0.59, similar to the value of 0.56 seen in the laboratory experiments. By summing all changes of pore occupancy from one scan to the next which occurred over 1 h (see Fig. 8) the percentage of the change in phase occupancy within 1 h was 26%.

The percentage of fluid rearrangement using the synchrotron is 7% lower than that obtained using laboratory-based micro-CT, representing a fractional decrease of 24%. While this is not a big difference, there might be three reasons for this. First, these two experiments were conducted on two different samples. However, Bentheimer sandstone is homogeneous and the pore size distributions of the two samples were almost identical. Second, the procedures of these two experiments were different. In the laboratory-based micro-CT experiment, more brine was injected as the fractional flow was increased at a fixed total flow rate, until steady state was reached. However, in fast synchrotron micro-CT, the flow rates of oil and brine were increased with a fixed $f_w = 0.5$. Finally, the scan time and the image quality could make a difference in our quantification of intermittency. Specifically, the synchrotron images were generally of poorer quality, since we wished to acquire scans quickly, and as a result we may have underestimated the degree of intermittency by misidentifying intermediate grayscales.

In conclusion, the flow regimes identified using fast synchrotron images are consistent with the results we observed from a laboratory micro-CT scanner.

E. Phase diagrams

To perform further quantitative analysis of flow regimes and compare with other experiments to the literature, we now define wetting- and nonwetting-phase capillary numbers as follows [10,11]:

$$Ca_w = \frac{q_w \mu_w}{\sigma} \quad (3)$$

and

$$Ca_{nw} = \frac{q_{nw} \mu_{nw}}{\sigma}, \quad (4)$$

respectively, where q is the Darcy velocity [m/s], μ is the dynamic viscosity [Pa s], and σ is the interfacial tension between the wetting and nonwetting phases [N/m].

We vary capillary numbers over a range of Ca_w and Ca_{nw} , as shown in Table II, and summarize our results in the phase diagram shown in Fig. 9. At very low capillary numbers, the nonwetting phase flows through constant and connected 3D

TABLE II. Wetting and nonwetting phase capillary numbers for the experiments presented in this work.

| q_t (ml/min) | 0.02 | 0.04 | 0.08 | 0.4 | 0.8 | 1.2 | 2.5 | 4 |
|--------------------------|------|------|------|------|------|------|-------|-------|
| $Ca \times 10^{-7}$ | 2.1 | 4.2 | 8.3 | 42.0 | 83.0 | 130 | 260 | 420 |
| $Ca_w \times 10^{-7}$ | 1.1 | 2.1 | 4.2 | 21.2 | 41.8 | 65.5 | 131.5 | 211.5 |
| $Ca_{nw} \times 10^{-7}$ | 1.0 | 2.1 | 4.1 | 20.8 | 41.2 | 64.5 | 128.5 | 208.5 |

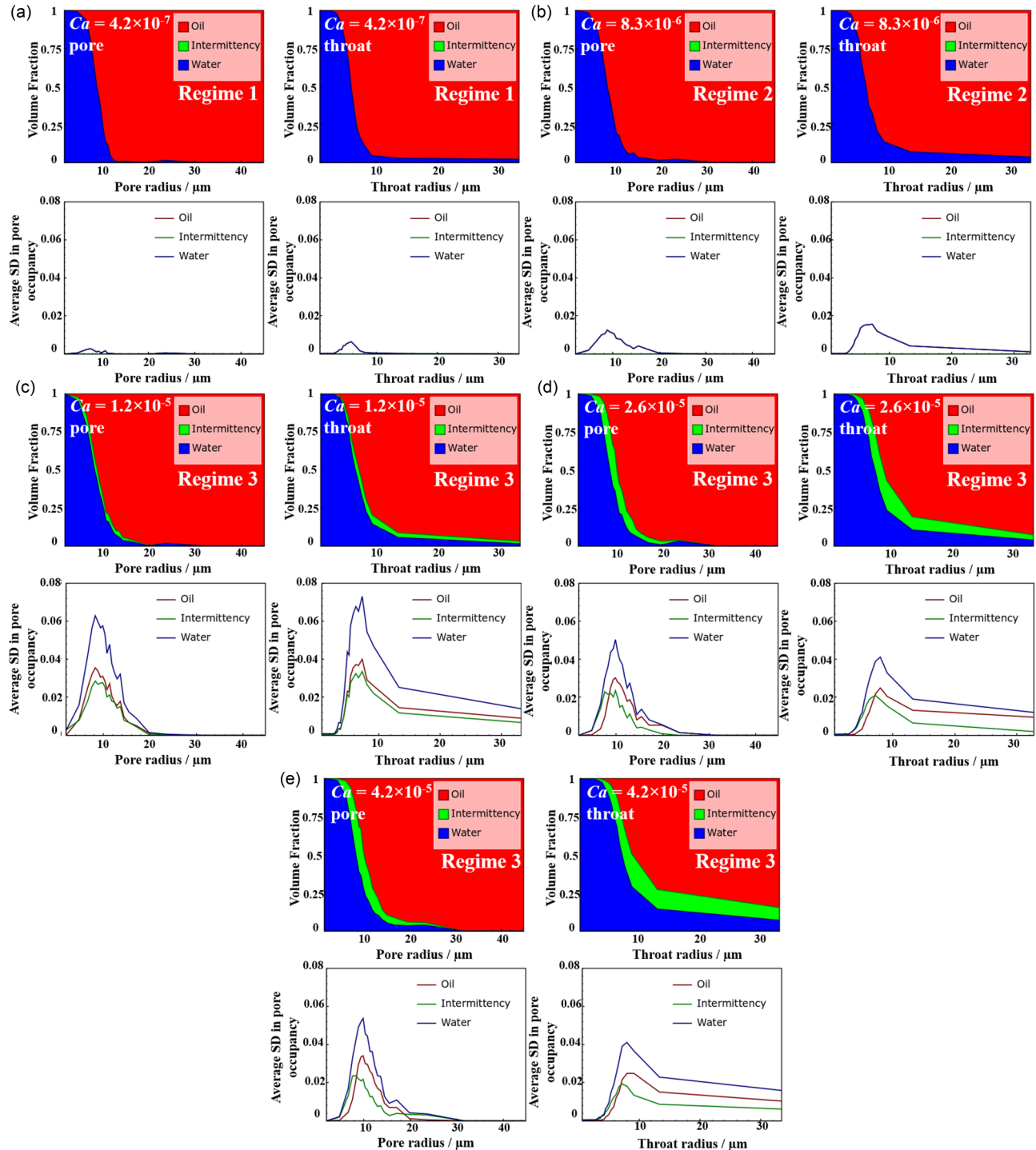


FIG. 8. The volume fraction of pore/throat radii occupied by oil, brine, and intermittency as a function of radius when Ca is 4.2×10^{-7} , 8.3×10^{-6} , 1.2×10^{-5} , 2.6×10^{-5} , and 4.2×10^{-5} . Red is oil, green is the intermittency (type 2), and blue represents brine. The lower figures show the standard deviation, SD, in individual pore occupancy between the scans in the last 20 min of steady-state flow, indicating the amount of type 1 oil and water intermittency or variations in type 2 intermittent regions.

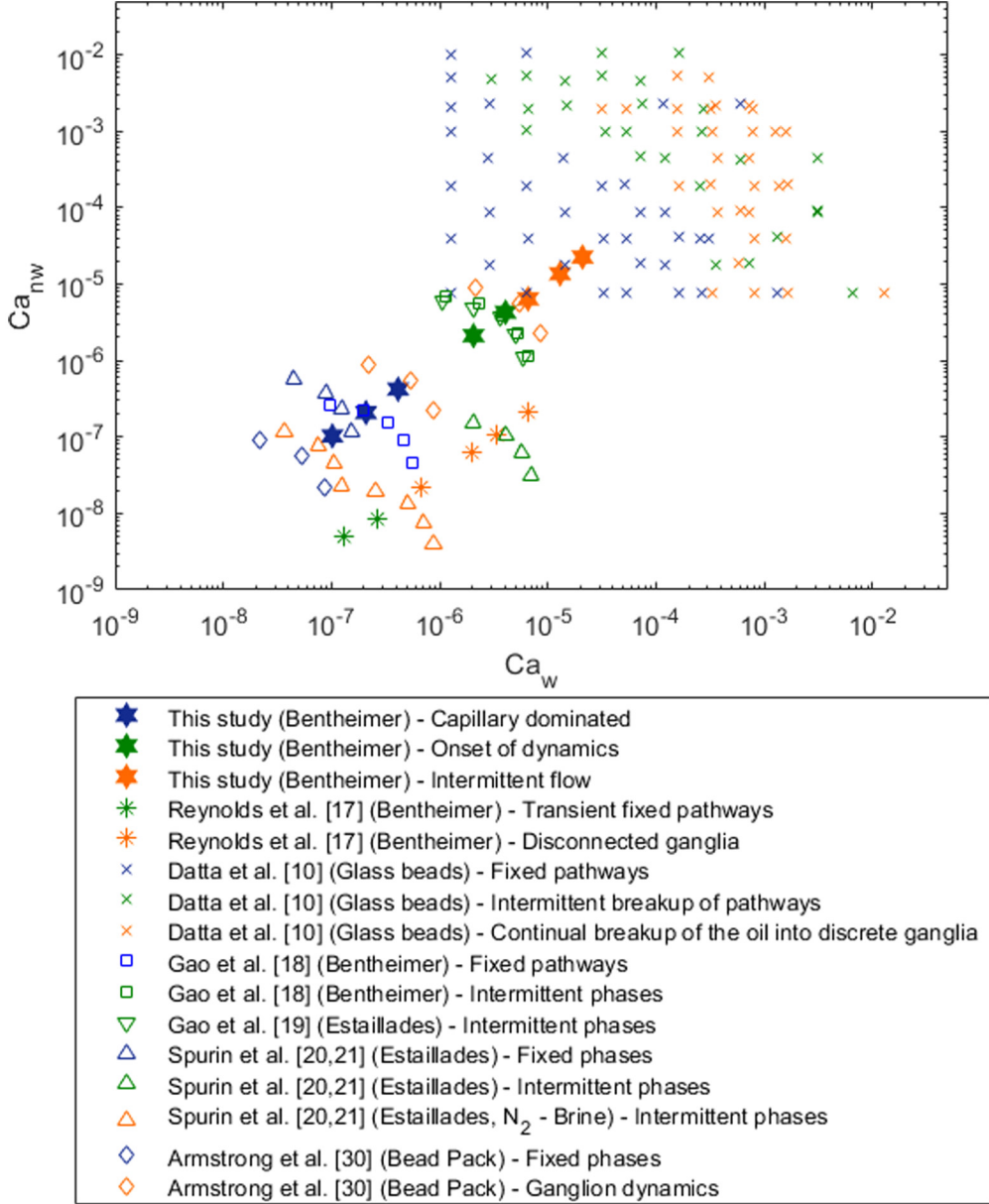


FIG. 9. State diagram of the transition from flow with stable pathways to flow with dynamic connectivity for simultaneous two-phase flow through Bentheimer as a function of Ca_w and Ca_{nw} . Blue (black) represents regime 1 (capillary controlled). Green (dark gray) represents regime 2 (onset of dynamics). Red (light gray) represents regime 3 (intermittent regime).

pathways in porous media, shown by the blue symbols. When Ca_w or/and Ca_{nw} increase, we see the onset of dynamics, regime 2, shown by the green symbols. At very high Ca_w or/and Ca_{nw} , the nonwetting phase has more frequent rearrangement and continually breaks up into discrete ganglia, shown by the red symbols.

As shown in Fig. 9, the first class of connected-to-broken-up transition occurs when Ca_w exceeds a threshold value, $\text{Ca}^* \approx 10^{-6}$, and the second class transition is estimated as $\text{Ca}^i \approx 10^{-5}$ where $\text{Ca}_w/\text{Ca}_w^i + \text{Ca}_{nw}/\text{Ca}_{nw}^i \sim \text{const}$ is summarized from this study.

We have compared our results with work from Datta *et al.* [10], Reynolds *et al.* [17], and Spurin *et al.* [20,21]. Datta *et al.* [10] studied brine-oil flow in cuboid packs of glass beads with a cross-sectional area 9 mm² and length of 2 cm at capillary

numbers 10⁻⁶ to 10⁻¹ at ambient condition. Reynolds *et al.* [17] conducted the study of brine-N₂ flow in cylindrical Bentheimer samples with a diameter of 4 mm and length of 4 cm at capillary numbers 10⁻⁸ to 10⁻⁵ at 10 MPa and 50 °C. Spurin *et al.* [20,21] examined both brine-oil at ambient conditions and brine-N₂ at 10 MPa flow in a cylindrical Estailades sample with 6 mm diameter and 21 mm length at capillary numbers 10⁻⁸ to 10⁻⁶. Armstrong *et al.* [31] conducted study on brine-oil flow in a cylindrical pack of glass beads, Robuglas, with a diameter of 4 mm and length of 20 mm at capillary numbers 10⁻⁷ to 10⁻⁵ at ambient conditions. Details of these experiments are listed in Table III.

As shown in Fig. 9, it is clear that the critical capillary numbers from Datta *et al.* [10] are larger than those from our analysis, while our critical capillary numbers are larger

TABLE III. Comparison of Ca values between this work and previously published studies.

| Author | Fluid system | Sample | Porosity | Area (mm ²) | Length (mm) | Ca _w range | Ca _{nw} range |
|------------------------------|-----------------------|------------|----------|-------------------------|-------------|------------------------------------|------------------------------------|
| This work | Oil-brine | Bentheimer | 0.20 | 28.3 | 57 | 10 ⁻⁷ –10 ⁻⁴ | 10 ⁻⁷ –10 ⁻⁴ |
| Datta <i>et al.</i> [10] | Oil-brine | Bead pack | 0.41 | 9 | 20 | 10 ⁻⁶ –10 ⁻¹ | 10 ⁻⁵ –10 ⁻¹ |
| Reynolds <i>et al.</i> [17] | N ₂ -brine | Bentheimer | 0.19 | 12.6 | 40 | 10 ⁻⁷ –10 ⁻⁵ | 10 ⁻⁸ –10 ⁻⁶ |
| Gao <i>et al.</i> [18] | Oil-brine | Bentheimer | 0.22 | 19.6 | 60 | 10 ⁻⁸ –10 ⁻⁶ | 10 ⁻⁸ –10 ⁻⁶ |
| Gao <i>et al.</i> [19] | Oil-brine | Estailades | 0.28 | 28.3 | 51 | 10 ⁻⁷ –10 ⁻⁶ | 10 ⁻⁷ –10 ⁻⁶ |
| Spurin <i>et al.</i> [20,21] | Oil-brine | Estailades | 0.29 | 28.3 | 21 | 10 ⁻⁹ –10 ⁻⁸ | 10 ⁻⁹ –10 ⁻⁸ |
| Spurin <i>et al.</i> [20,21] | N ₂ -brine | Estailades | 0.29 | 28.3 | 21 | 10 ⁻⁸ –10 ⁻⁷ | 10 ⁻⁹ –10 ⁻⁷ |
| Armstrong <i>et al.</i> [31] | Oil-brine | Bead pack | 0.33 | 12.6 | 20 | 10 ⁻⁸ –10 ⁻⁶ | 10 ⁻⁸ –10 ⁻⁶ |

than those obtained from Reynolds *et al.* [17]. The difference in critical capillary numbers in these experiments can be ascribed to different pore structure heterogeneity in a beadpack and sandstone [34] and different fluid pairs. For instance, in Spurin *et al.* [21] it was shown that the flow regime was a function both of capillary number and mobility ratio, with more intermittency observed when the nonwetting phase was much less viscous than the wetting phase.

Here we use the Reynolds number [4,35], a dimensionless number used to indicate the transition from viscous to inertial dominated flows, to help identify the differences in flow behavior seen in these experiments. The Reynolds number is the ratio of inertial forces to viscous forces and is defined as $Re = \rho q L / \phi \mu$, where ρ is the density of the fluid, q is the Darcy velocity in this context, L is the characteristic length, ϕ is the porosity, and μ is the dynamic viscosity. The characteristic length, quantified in Table IV, is a representative pore length, or distance between throats, which is calculated from a pore-network analysis of the pore structure [32]. As with capillary number, the Reynolds number can be separately defined for each phase.

While, in all cases that we studied, the flow regime is laminar, we will use the Reynolds number, and specifically its dependence on fluid viscosity and characteristic length, to evaluate the ratio of inertial to viscous forces and help explain the difference in critical capillary numbers for intermittent flow. As Fig. 10 shows, the Reynolds numbers for both wetting phase and nonwetting phase were less than 1, which proves that inertial effects are, on average, small. Except for the Reynolds numbers from Datta *et al.* [10], the boundary for intermittent flow (regime 3) occurs at approximately $Re_{w/nw} \approx 2 \times 10^{-2}$. However, again we do not see a clear segregation of the results, indicating that the transition to intermittent flow is governed by geometric and mobility factors that are encapsulated in neither Ca nor Re. While there is a wide range of local flow speed within heterogeneous porous media [34,38], which may lead to individual pores where Re exceeds 1, there is no evidence that the onset of intermittency can be quantified by the emergence of inertial effects at the pore scale.

Finally we consider the Weber number [36], which is the ratio of the inertial force to the interfacial force and defined as $We = \rho q^2 L / \phi \sigma$, where ρ is the density of the fluid, q is the Darcy velocity in this context, L is the characteristic length, ϕ is the porosity, and σ is the interfacial tension. Again We is defined for each phase. Figure 11 shows the phase diagram as a function of We_w and We_{nw}. In all the experiments We is much less than 1, indicating that inertial forces are very weak compared to interfacial tension effects. Again, there is no clear delineation of flow regimes, supporting the hypothesis that intermittency is not controlled by inertial forces, but by pore-scale geometry and mobility not simply quantified by a single characteristic length.

While there is uncertainty in our estimates of Reynolds and Weber numbers, largely due to ambiguities in the estimate of a characteristic pore length, it is unlikely that this accounts for the scatter in the data. Some other features of the pore space and fluids are needed for a more quantitative delineation of flow regimes.

The impact of porous media heterogeneity, ignored in our dimensionless numbers, has been shown to be crucial in assessing the impact of viscous forces on the onset of inertial flow during single-phase flow in a beadpack, sandstone, and carbonate by Muljadi *et al.* [34]. We suggest that heterogeneity and fluid mobility also control the onset of intermittent multiphase flow. Intermittency itself is governed by the competition between viscous and capillary forces, which can be explained by considering an energy balance where the energy introduced by injecting the fluids is matched by the creation of new interfaces to create intermittent connections [17,22]: inertial effects appear to be small in our experiments. This observation has already been made in the context of the mobilization of trapped ganglia by viscous forces [37]. Further work is required to provide a prediction of the onset of intermittency in different porous media.

IV. CONCLUSIONS

Co-injection using *n*-decane and brine was performed at a fixed fractional flow of 0.5 for a range of capillary numbers

TABLE IV. The characteristic length estimated for each sample.

| Rock type | Bentheimer | Estailades | Glass beads [10] | Glass beads [10] | Glass beads [31] |
|-----------|------------|------------|------------------|------------------|------------------|
| L (μm) | 150 | 63 | 25 | 41 | 24.6 |

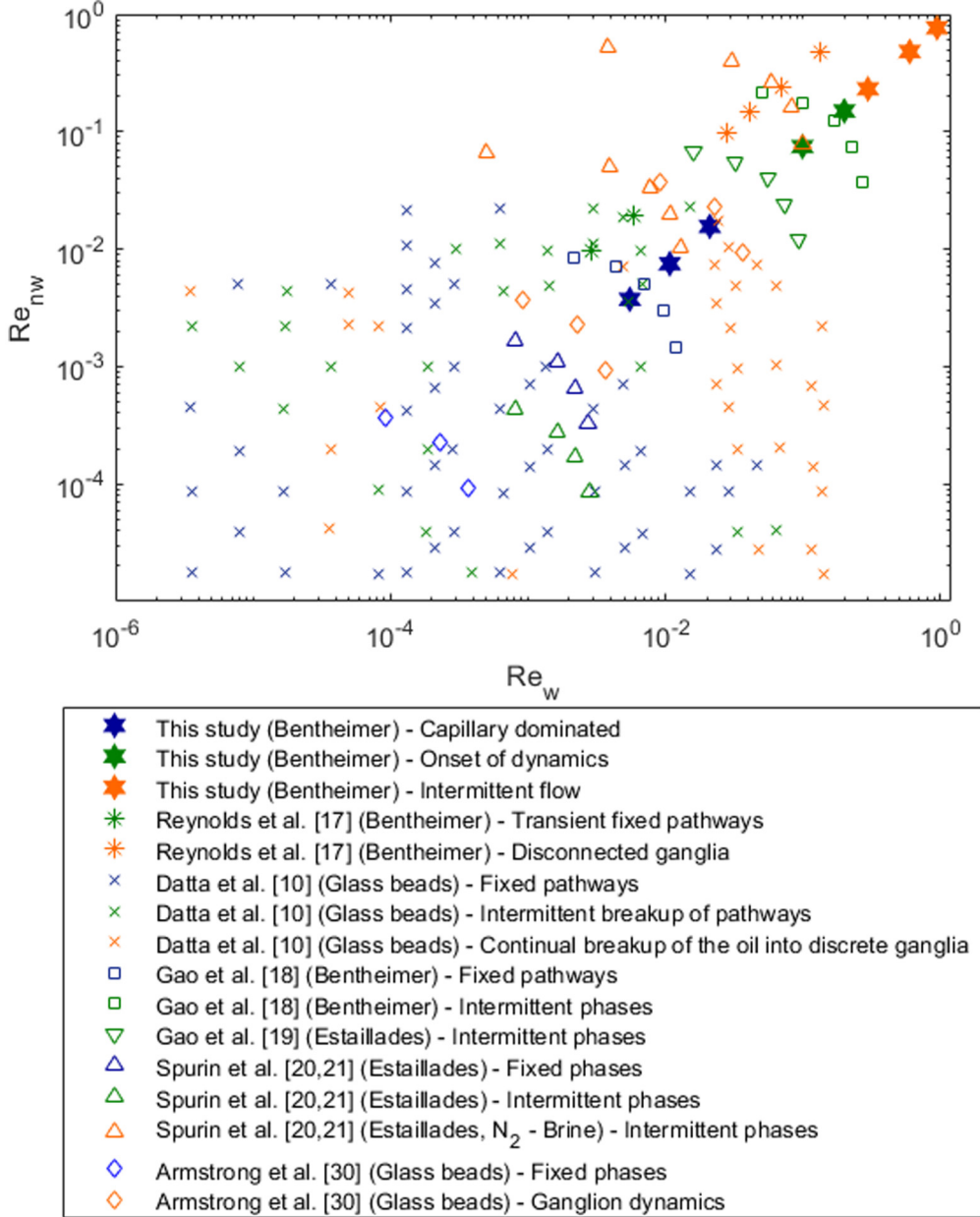


FIG. 10. State diagram of the transition from flow with stable pathways to flow with dynamic connectivity for simultaneous two-phase flow as a function of Re_w and Re_{nw} . Blue (black) represents regime 1 (capillary controlled). Green (dark gray) represents regime 2 (onset of dynamics). Red (light gray) represents regime 3 (intermittent regime).

$2.1 \times 10^{-7} \leq Ca \leq 4.2 \times 10^{-5}$. We have studied the connectivity and flow dynamics for the regimes identified in previous work [22]. At the lowest flow rates, when the capillary number is less than $Ca^* \approx 10^{-6}$, the traditional multiphase Darcy law, Eq. (1), is valid, and both phases follow fixed flow pathways. When capillary number increases to $Ca^* \approx 10^{-6}$, we see the onset of dynamics when there is an additional energy supplied to the system which allows the creation of new interfaces. The oil phase starts to intermittently connect and disconnect in additional places, and the oil saturation starts to decrease while there is almost no change of the total mobility. When the capillary number increases beyond a critical $Ca^i \approx 10^{-5}$, an increased overall flow conductance is caused by intermittent

flow at steady state. In this regime the relationship between capillary number and pressure gradient becomes nonlinear. This is associated with rapid, subminute fluctuations in pore-scale occupancy.

At low Ca , connected pathways of ganglia were fixed and the proportions of small, medium, and large ganglia were constant. However, with an increase in Ca we saw an intermittent formation and break-up of oil ganglia. This changed dynamic connectivity, which resulted in fluctuating larger and medium-sized ganglia populations, while the small ganglia sizes stayed constant over time. Furthermore, we find that most of dynamic connectivity resulting in formation of an intermittent phase occurs in the pores and throats of intermediate size. When

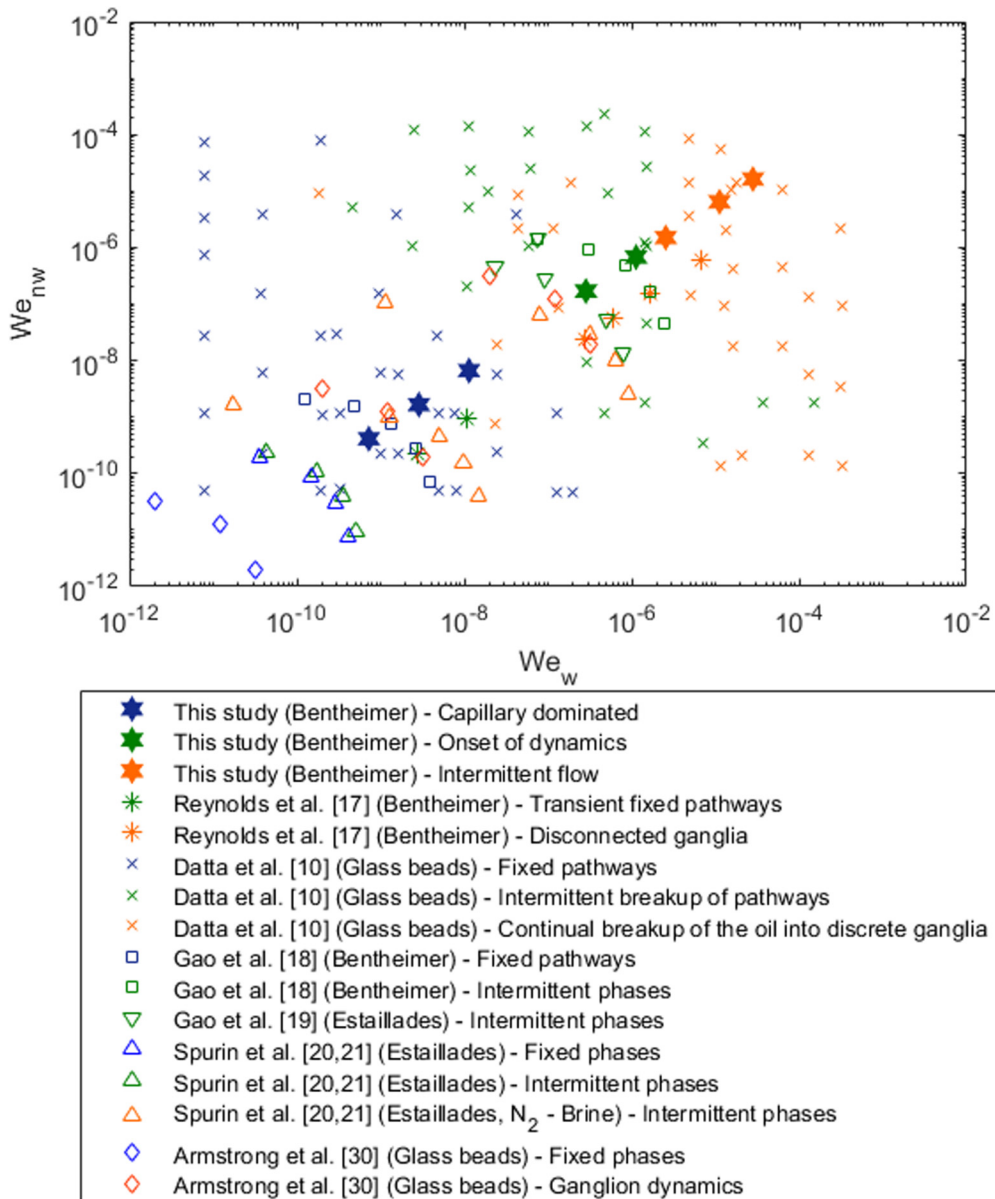


FIG. 11. State diagram of the transition from flow with stable pathways to flow with dynamic connectivity for simultaneous two-phase flow as a function of We_w and We_{nw} . Blue (black) represents regime 1 (capillary controlled). Green (dark gray) represents regime 2 (onset of dynamics). Red (light gray) represents regime 3 (intermittent regime).

Ca increased, the fraction of intermittent phase increased and spread to a wider range of pore/throat sizes.

To characterize the topology of the nonwetting phase ganglia, we computed the Euler characteristic. This initially decreased with flow rate with the onset of dynamics, showing that overall the formation of new pathways leads to better connectivity of the nonwetting phase. At higher flow rates, in the intermittent regime, the Euler characteristic increased, as nonwetting phase ganglia were broken up and, at any instant, the nonwetting phase appeared disconnected.

Capillary, Reynolds, and Weber numbers of the wetting phase and the nonwetting phase have been calculated and plotted on regime diagrams to compare the importance of the capillary, viscous, and inertial forces on intermittent flow. We demonstrate that inertial forces are, on average, small at

the onset of intermittency. However, the flow regimes are not simply delineated by these dimensionless numbers, indicating that intermittency is also controlled by the heterogeneity of the porous medium and fluid mobility.

Overall, dynamic connectivity as a displacement mechanism can aid rates of enhanced oil recovery, carbon dioxide storage, and remediation or management of nonaqueous liquid contaminants in aquifers. Future work is needed to quantify the flow regimes for different rock types, wettabilities, and fluids, as well as explore the implications of dynamic connectivity for different porous media processes.

ACKNOWLEDGMENTS

We gratefully acknowledge funding from the Qatar Carbonates and Carbon Storage Research Centre (QCCSRC),

provided jointly by Qatar Petroleum, Shell, and the Qatar Science & Technology Park. We thank the Diamond Light Source for access to beamline I13, and Dr. Christoph Rau, Dr. Shashidhara Marathe, and Dr. Kaz Wanelik for their

assistance. We also thank the additional members of the experimental team from Imperial College, including Dr. Amer Alhammadi, Dr. Kamaljit Singh, Dr. Qingyang Lin, Dr. Yousef A. Al-Khulaifi, and Dr. Hannah Menke.

-
- [1] S. Bachu, *Environ. Geol.* **44**, 277 (2003).
 - [2] N. Morrow and J. Buckley, *J. Pet. Technol.* **63**, 106 (2011).
 - [3] M. Andrew, B. Bijeljic, and M. J. Blunt, *Int. J. Greenhouse Gas Control* **22**, 1 (2014).
 - [4] M. J. Blunt, *Multiphase Flow in Permeable Media: A Pore-Scale Perspective* (Cambridge University Press, Cambridge, 2017).
 - [5] D. Avraam and A. Payatakes, *J. Fluid Mech.* **293**, 207 (1995).
 - [6] D. Avraam and A. Payatakes, *Transp. Porous Media* **20**, 135 (1995).
 - [7] K. T. Tallakstad, G. Løvoll, H. A. Knudsen, T. Ramstad, E. G. Flekkøy, and K. J. Måløy, *Phys. Rev. E* **80**, 036308 (2009).
 - [8] K. T. Tallakstad, H. A. Knudsen, T. Ramstad, G. Løvoll, K. J. Måløy, R. Toussaint, and E. G. Flekkøy, *Phys. Rev. Lett.* **102**, 074502 (2009).
 - [9] S. Sinha and A. Hansen, *Europhys. Lett.* **99**, 44004 (2012).
 - [10] S. S. Datta, J.-B. Dupin, and D. A. Weitz, *Phys. Fluids* **26**, 062004 (2014).
 - [11] S. S. Datta, T. Ramakrishnan, and D. A. Weitz, *Phys. Fluids* **26**, 022002 (2014).
 - [12] D. Wildenschild and A. P. Sheppard, *Adv. Water Resour.* **51**, 217 (2013).
 - [13] S. Berg, R. Armstrong, A. Georgiadis, H. Ott, A. Schwing, R. Neiteler, N. Brussee, A. Makurat, M. Rucker, L. Leu *et al.*, *Petrophysics* **56**, 15 (2015).
 - [14] M. Rucker, S. Berg, R. Armstrong, A. Georgiadis, H. Ott, A. Schwing, R. Neiteler, N. Brussee, A. Makurat, L. Leu *et al.*, *Geophys. Res. Lett.* **42**, 3888 (2015).
 - [15] S. Berg, R. Armstrong, H. Ott, A. Georgiadis, S. A. Klapp, A. Schwing, R. Neiteler, N. Brussee, A. Makurat, L. Leu *et al.*, *Petrophysics* **55**, 304 (2014).
 - [16] S. Berg, M. Rucker, H. Ott, A. Georgiadis, H. Van der Linde, F. Enzmann, M. Kersten, R. Armstrong, S. De With, J. Becker *et al.*, *Adv. Water Resour.* **90**, 24 (2016).
 - [17] C. A. Reynolds, H. Menke, M. Andrew, M. J. Blunt, and S. Krevor, *Proc. Natl. Acad. Sci. USA* **114**, 8187 (2017).
 - [18] Y. Gao, Q. Lin, B. Bijeljic, and M. J. Blunt, *Water Resour. Res.* **53**, 10274 (2017).
 - [19] Y. Gao, A. Q. Raeini, M. J. Blunt, and B. Bijeljic, *Adv. Water Resour.* **129**, 56 (2019).
 - [20] C. Spurin, T. Bultreys, B. Bijeljic, M. J. Blunt, and S. Krevor, *Phys. Rev. E* **100**, 043103 (2019).
 - [21] C. Spurin, T. Bultreys, B. Bijeljic, M. J. Blunt, and S. Krevor, *Phys. Rev. E* **100**, 043115 (2019).
 - [22] Y. Gao, Q. Lin, B. Bijeljic, and M. J. Blunt, *Phys. Rev. Fluids* **5**, 013801 (2020).
 - [23] J. Andreas, E. Hauser, and W. Tucker, *J. Phys. Chem.* **42**, 1001 (2002).
 - [24] C. E. Stauffer, *J. Phys. Chem.* **69**, 1933 (1965).
 - [25] Avizo, www.vsg3d.com.
 - [26] W. Burger and M. J. Burge, *Principles of Digital Image Processing: Core Algorithms* (Springer, 2009).
 - [27] W. Burger and M. J. Burge, *Digital Image Processing: An Algorithmic Introduction Using Java* (Springer, 2016).
 - [28] Q. Lin, Y. Al-Khulaifi, M. J. Blunt, and B. Bijeljic, *Adv. Water Resour.* **96**, 306 (2016).
 - [29] A. Buades, B. Coll, and J.-M. Morel, in *2005 IEEE Computer Society Conference on Computer Vision and Pattern Recognition (CVPR'05)* (IEEE, New York, 2005), Vol. 2, pp. 60–65.
 - [30] A. Buades, B. Coll, and J.-M. Morel, *Int. J. Comput. Vision* **76**, 123 (2008).
 - [31] R. T. Armstrong, J. E. McClure, M. A. Berrill, M. Rücker, S. Schlüter, and S. Berg, *Phys. Rev. E* **94**, 043113 (2016).
 - [32] A. Q. Raeini, B. Bijeljic, and M. J. Blunt, *Phys. Rev. E* **96**, 013312 (2017).
 - [33] T. Bultreys, Q. Lin, Y. Gao, A. Q. Raeini, A. AlRatrou, B. Bijeljic, and M. J. Blunt, *Phys. Rev. E* **97**, 053104 (2018).
 - [34] B. P. Muljadi, M. J. Blunt, A. Q. Raeini, and B. Bijeljic, *Adv. Water Resour.* **95**, 329 (2016).
 - [35] Z. Zeng and R. Grigg, *Transp. Porous Media* **63**, 57 (2006).
 - [36] A. Frohn and N. Roth, *Dynamics of Droplets* (Springer Science & Business Media, 2000).
 - [37] P. Amili and Y. Yortsos, *Transp. Porous Media* **64**, 25 (2006).
 - [38] B. Bijeljic, A. Raeini, P. Mostaghimi, and M. J. Blunt, *Phys. Rev. E* **87**, 013011 (2013).